Supporting Information for

Valence Band of Rutile TiO_2(110) Investigated by Polarized Light Based Angle-Resolved Photoelectron Spectroscopy

Shanshan Dong,[a, d] Shucai Xia,[a, d] Chao Wang,[b] Jingwei Dong,[a] Tianjun Wang,[a] Rui Li,[b] Zefeng Ren,[a] Dongxu Dai,[a] Xueming Yang[a, c], Chuanyao Zhou[a*]

a. State Key Laboratory of Molecular Reaction Dynamics, Dalian Institute of Chemical Physics, Chinese Academy of Science, 457 Zhongshan Road, Dalian, 116023, Liaoning, P. R. China

b. School of Optoelectronic Engineering and Instrumentation Science, Dalian University of Technology, Ganjingzi District, Dalian, 116024, Liaoning Province, P. R. China

c. Department of Chemistry, Southern University of Science and Technology, 1088 Xueyuan Road, Shenzhen, Guangdong, 518055, P. R. China

d. University of Chinese Academy of Sciences, No.19A Yuquan Road, Shijingshan District, 100049, Beijing, P. R. China

*) To whom all correspondence should be addressed:

chuanyaozhou@dicp.ac.cn

Tel: +86-411-84379701

Fax: +86-411-84675584

Content

1. Experimental Details

The ARPES experiments were performed in a μ-metal UHV chamber (base pressure <3 × 10^{-10} mbar) which is equipped with standard sample preparation and characterization devices. TiO_2(110) sample (10×5×1 mm^3, HF-Kejing), which was fixed on a grounded tantalum plate, was placed at the end of a five-axes manipulator, ensuring the X, Y and Z translation and polar and azimuthal rotation (around Z axis and the sample surface normal, respectively). It was cleaned by cycles of Ar^+ sputtering and UHV annealing at 850 K, and the quality was confirmed by the sharp (1×1) low electron energy diffraction (LEED) pattern and undetectable contamination in the Auger electron spectroscopy. The electrical connection of the bulk reduced TiO_2 substrate and the tantalum plate aligns the Fermi level.

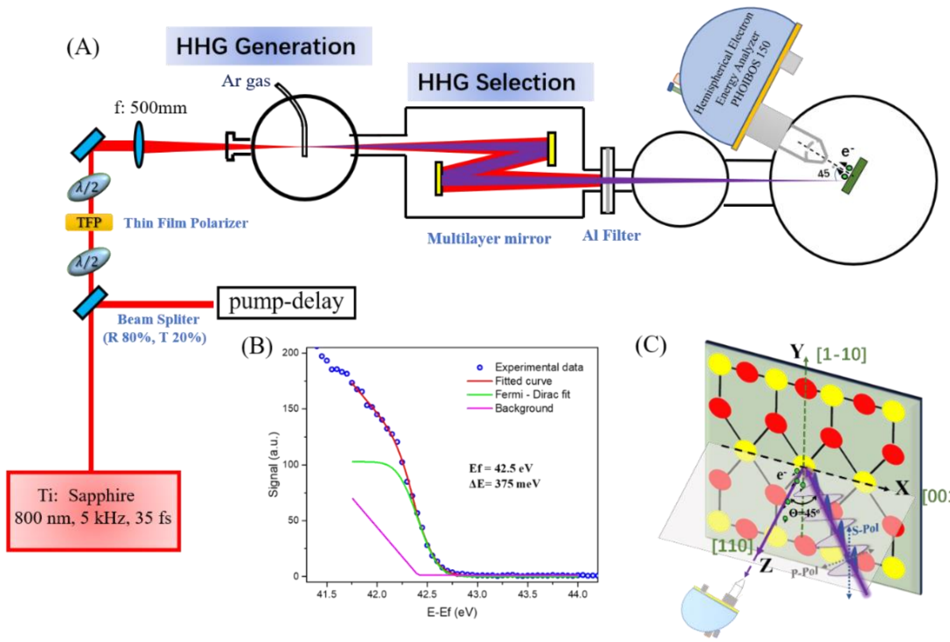

Figure S1. Schematic experimental configuration. (A) Optical layout for high-order harmonic generation and selection. (B) Overall energy resolution measured from a polycrystalline gold sample at 300 K. (C) Configuration of the TiO_2(110) sample, the electron energy analyzer and the polarization of the EUV light.

The EUV (extreme ultraviolet) light was produced through high-order harmonic generation (HHG) (Figure S1A), where 0.8 mJ output (800 nm, 35 fs, 5000 Hz) from a regenerative amplifier (Legend Elite Duo HE-USP; Coherent, Inc) was focused onto a stainless steel tube in the generation chamber. Ar gas was chosen as the media for HHG and the pressure was actively regulated by a mass controller. The resulted high-order harmonics propogate collinearly with the driving laser and pass through a two-mirror monochromator where the 27^{th} order harmonic is selected. After transmitting the 200-nm thick aluminum foil, the selected EUV light was focused onto the TiO_2 sample surface at an incident angle of 45 degree.

Photoelectrons were collected by a hemispherical electron energy analyzer (Phoibos 150; SPECS) combined with a two-dimensional CCD camera. All the ARPES experiments were carried out at a sample temperature of 300 K to prevent residual H_2O adsorption. The pass energy was set to 20 eV and the overall energy resolution was measured to be 375 meV from a polycrystalline gold sample (Figure S1B). The photon flux of the selected EUV, which could be tuned by varying the driving laser power, the focal condition and the Ar gas pressure, was optimized to maintain no space charge effect. The photon energy was then fitted by Fermi-Dirac distribution of the Fermi edge of the polycrystalline gold sample to be 42.5 eV. Polarization of the resulted EUV light, which follows that of the driving laser, could be changed by rotating the half wave plate in the optical path for 800 nm laser. Schematic configuration of the $TiO_2(110)$ sample, the electron energy analyzer and the polarization of the EUV light are shown in Figure S1C. The EUV light, the surface normal and the electron energy analyzer are placed in the XZ (horizontal) plane. The entrance slit of the analyzer was located along the X axis, enabling the measurement of momentum-resolved electronic structure along this direction. P- and S-polarization mean that the electric field of the incident EUV light are along and perpendicular to the XZ plane, respectively.

2. Molecular-orbital Bonding Structure and the Coordinate of Octahedral TiO_6 for Rutile TiO_2

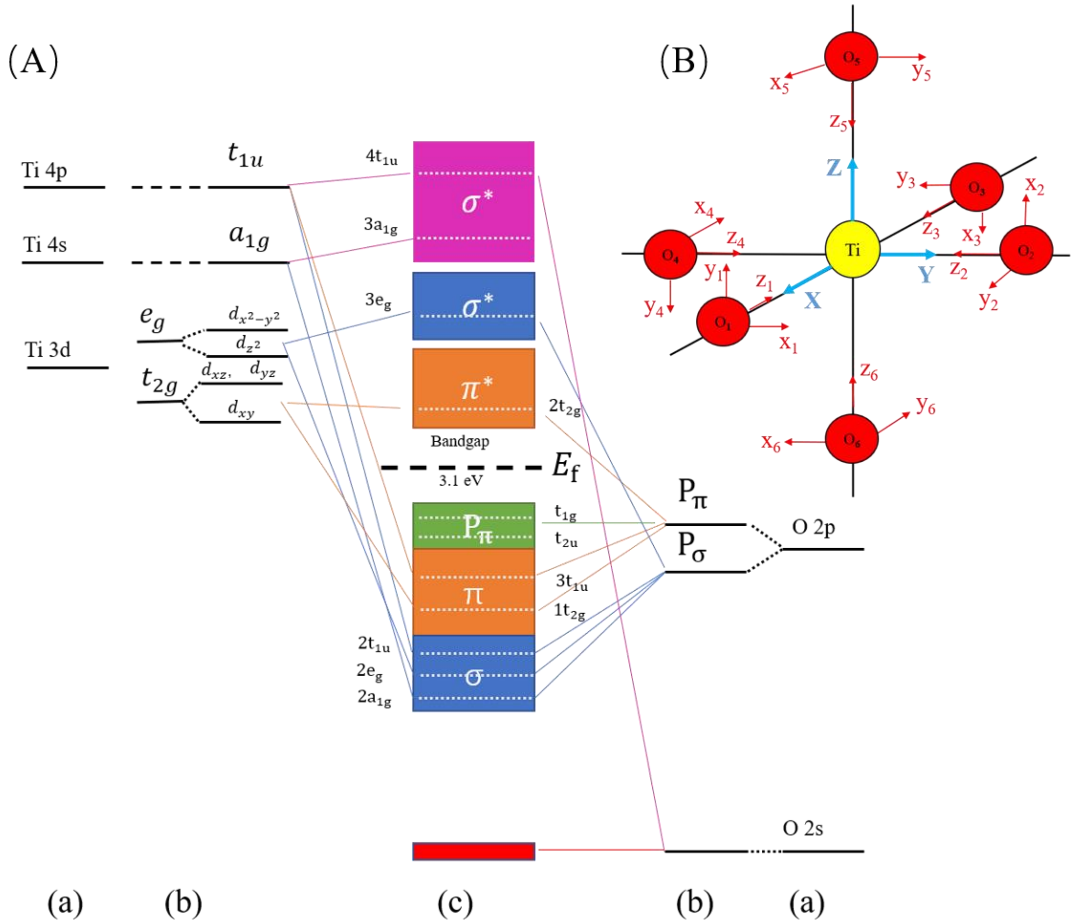

Figure S2. (A) Molecular-orbital bonding structure for Rutile TiO_2, (a) Ti atom levels, (b)crystal-field split levels, and (c) final interaction states. (B)The inset picture is the coordinate of octahedral TiO_6.[1]

3. Accessible $k_{\perp}$ at $h\upsilon$=42.5 eV

In a photoemission process from a crystal surface, the parallel component of the wavevector ($k_{\|}$) is conserved but the perpendicular one ($k_{\perp}$) is not. Then energy and parallel momentum conservation can be expressed as equation (1-3).[2-3]

$$k_{\|} = \sqrt{\frac{2m_0 \times E_{kin}}{\hbar^2}} \sin\theta \qquad (1)$$

$$k_{\perp} = \sqrt{\frac{2m^*}{\hbar^2}} \sqrt{E_{kin}(\cos\theta)^2 + V_0} \qquad (2)$$

$$E_{kin} = h\upsilon - \Phi - E_B \qquad (3)$$

Where θ is the emission angle, and E_{kin} is kinetic energy of the emitted free electrons with mass m_0. The effective mass m^* of the electrons is approximately 1.35 m_0.[4-5] V_0 is inner potential parameter with respect to the Fermi energy, and its value is about 15 eV.[4-5] Φ is work function, which is approximately 4.8 eV for rutile TiO_2(110).[6] E_B is the binding energy, which is between 0 and 10 eV in this work. According to equation 2, the accessible $k_{\perp}$ is between 0.390 and 0.433 Å^{-1} with a photon energy of 42.5 eV. For rutile TiO_2, ΓM = 0.485 Å^{-1}. Therefore, the bands we measured are close to rather than exactly in the surface Brillouin zone.

4. Determination of VBM's along $\overline{\mathbf{\Gamma M}}$ and $\overline{\mathbf{\Gamma Z}}$

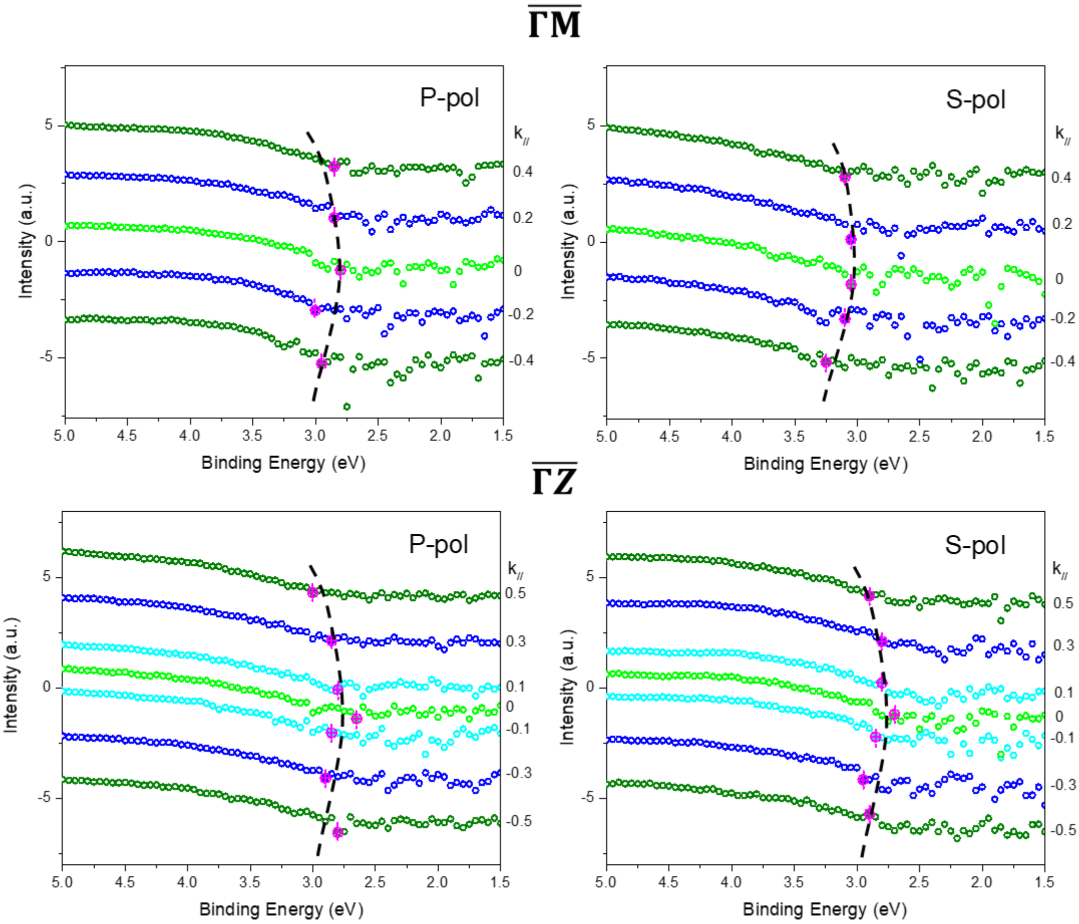

Figure S3. Momentum-integrated (in 0.1 $Å^{-1}$ range) EDC from Figure 1C-1F. The VBM along $\overline{\mathbf{\Gamma M}}$ (k=-0.4~0.4 (**1/Å**)) and $\overline{\mathbf{\Gamma Z}}$ (k=-0.5~0.5 (**1/Å**)) are determined by the kink of the spectra in the logarithmic representation.[7]

5. Spectra at $\bar{\Gamma}$, $\bar{\mathrm{M}}$ and $k_{//}$=0.5 Å^{-1}

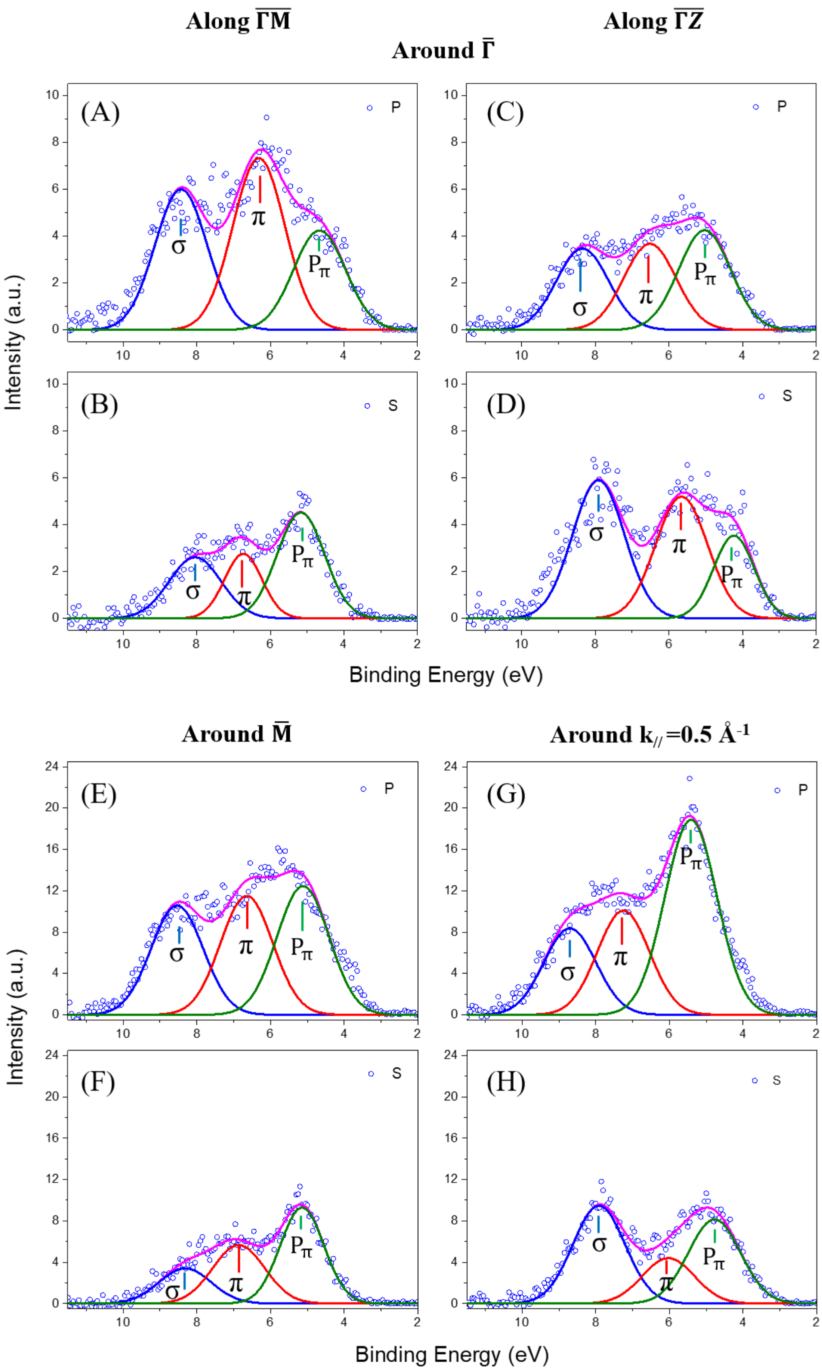

Figure S4. Momentum-integrated (in 0.01 Å^{-1} range) EDC from Figure 2C-2F. Left and right panels display the spectra along $\overline{\Gamma\mathrm{M}}$ and $\overline{\Gamma\mathrm{Z}}$ respectively. Polarization of the excitation EUV light are indicated in each graph. Spectra in A-D are normalized at the secondary electron edge, and those in E-H are normalized at E_B=20 eV.

Table S1. Fitted center (eV), fitted and predicted intensity of σ, π and P_π bands at $\bar{\Gamma}$ point as a function of high symmetry direction and excitation light polarization.

Obitals	Along $\overline{\mathbf{\Gamma M}}$ ($\bar{\mathbf{\Gamma}}$)						Along $\overline{\mathbf{\Gamma Z}}$ ($\bar{\mathbf{\Gamma}}$)					
	Center (eV)		**Measured Intensity**		**Predicted Intensity**		**Center (eV)**		**Measured Intensity**		**Predicted Intensity**	
	P	S	P	S	P	S	P	S	P	S	P	S
σ	8.42	8.04	1.00	0.43	1.00	0.44	8.34	7.91	0.58	0.98	1.03	0.28
π	6.31	6.73	1.22	0.33	0.94	0.63	6.52	5.66	0.61	0.87	0.88	0.56
P_π	4.66	5.17	0.71	0.69	0.39	0.26	5.03	4.24	0.71	0.46	0.32	0.32

Table S2. Fitted center (eV), fitted and predicted intensity of σ, π and P_π bands at specified point as a function of excitation light polarization.

Obitals	Along $\overline{\mathbf{\Gamma M}}$ ($\bar{\mathbf{M}}$)						Along $\overline{\mathbf{\Gamma Z}}$ ($\mathbf{k_{//}=0.5\ 1/Å}$)					
	Center (eV)		**Measured Intensity**		**Predicted Intensity**		**Center (eV)**		**Measured Intensity**		**Predicted Intensity**	
	P	S	P	S	P	S	P	S	P	S	P	S
σ	8.53	8.32	1.76	0.57	1.00	0.44	8.47	7.91	1.40	1.58	1.03	0.28
π	6.65	6.86	1.92	0.94	0.94	0.63	6.90	6.03	1.68	0.73	0.88	0.56
P_π	5.12	5.14	2.08	1.30	0.39	0.26	5.35	4.78	3.14	1.36	0.32	0.32

Fitted intensities are the relative peak area of the fitted bands. Predicted intensities are the relative detection efficiency of the molecular orbitals by $h\nu$=42.5 eV light in an ideal TiO_6 octahedron. Detailed calculations are described in the discussion section.

6. Previous ARPES Studies in the Surface/Bulk Brillouin Zone of Rutile TiO_2(110).

Table S3. Comparison between ARPES measured bands of rutile TiO_2. BZ stands for Brillouin zone. The values in the table are that at gamma points. The $k_{\perp}$ is between 0.390 and 0.433 Å^{-1} in our current work, close to rather than exactly in the surface Brillouin zone.

Along $\overline{\Gamma M}$ ($\bar{\Gamma}$)		**Along ΓM (Γ)**	**Along $\overline{\Gamma Z}$ ($\bar{\Gamma}$)**	
Surface BZ		**Bulk BZ**	**Surface BZ**	
Current work	Fischer et al's[4]	Raikar et al's[8]	Current work	Fischer et al's[4]
8.42 (σ_p)	/	8.77 (F)	8.43(σ_p)	8.44 (F)
8.06 (σ_s)	8.01 (F)	/	7.93 (σ_s)	/
6.72 (π_s)	6.85 (E)	7.24 (E)	6.64 (π_p)	7.26 (E)
6.31 (π_p)	/	6.34 (D)	5.78 (π_s)	6.06 (C)
5.20 ($P_{\pi s}$)	5.85 (C)	5.34 (C)	5.11($P_{\pi p}$)	/
4.67 ($P_{\pi p}$)	4.72 (B)	4.66 (B)	4.36 ($P_{\pi s}$)	4.74 (B)

7. The Predicted Detection Efficiency of σ, π, P_{π} Orbitals and Band Gap State.

Table S4. The predicted detection efficiency of σ orbitals. E, O and N correspond to even parity, odd parity, and no parity respectively.

σ			TiO_6-[110]				TiO_6-[1-10]			
	Orbitals		Incident plane//[1-10]		Incident plane//[001]		Incident plane//[1-10]		Incident plane//[001]	
$2A_{1g}$	Ti	O	P(E)	S(O)	P(E)	S(O)	P(E)	S(O)	P(E)	S(O)
σ1	4s	O_{1-4}, 2pz	E(√)E(√), E(√)	E(×)E(×), E(×)	E(√)E(√), E(√)	E(×)E(×), E(×)	E(√)E(√), E(√)	E(×)E(×), E(×)	E(√)E(√), E(√)	E(×)E(×), E(×)
			0.4	0	0.4	0	0.4	0	0.4	0
σ2	4s	O_{5-6}, 2pz	E(√)E(√), E(√)	E(×)E(×), E(×)	E(√)E(√), E(√)	E(×)E(×), E(×)	E(√)E(√), E(√)	E(×)E(×), E(×)	E(√)E(√), E(√)	E(×)E(×), E(×)
$2E_g$			0.4	0	0.4	0	0.4	0	0.4	0
σ3	$3dz^2$	O_{1-4}, 2pz	E(√)E(√), E(√)	E(×)E(×), E(×)	E(√)E(√), E(√)	E(×)E(×), E(×)	E(√)E(√), E(√)	E(×)E(×), E(×)	E(√)E(√), E(√)	E(×)E(×), E(×)
			0.6	0	0.6	0	0.6	0	0.6	0
σ4	$3dz^2$	O_{5-6}, 2pz	E(√)E(√), E(√)	E(×)E(×), E(×)	E(√)E(√), E(√)	E(×)E(×), E(×)	E(√)E(√), E(√)	E(×)E(×), E(×)	E(√)E(√), E(√)	E(×)E(×), E(×)
			0.6	0	0.6	0	0.6	0	0.6	0
σ5	$3dx^2$-y^2	O_{1-4}, 2pz	O(×)O(×), O(×)	O(√)O(√), O(√)	O(×)O(×), O(×)	O(√)O(√), O(√)	O(×)O(×), O(×)	O(√)O(√), O(√)	E(√)E(√), E(√)	E(×)E(×), E(×)
$2T_{1u}$			0	0.6	0	0.6	0	0.6	0.6	0
σ6	4px	$O_{1,3}$, 2pz	N(√)N(√), N(√)	N(√)N(√), N(√)	N(√)N(√), N(√)	N(√)N(√), N(√)	N(√)N(√), N(√)	N(√)N(√), N(√)	E(√)E(√), E(√)	E(×)E(×), E(×)
			0.4	0.4	0.4	0.4	0.4	0.4	0.4	0
σ7	4py	$O_{2,4}$, 2pz	N(√)N(√), N(√)	N(√)N(√), N(√)	N(√)N(√), N(√)	N(√)N(√), N(√)	N(√)N(√), N(√)	N(√)N(√), N(√)	E(√)E(√), E(√)	E(×)E(×), E(×)
			0.4	0.4	0.4	0.4	0.4	0.4	0.4	0
σ8	4pz	$O_{5,6}$, 2pz	E(√)E(√), E(√)	E(×)E(×), E(×)	E(√)E(√), E(√)	E(×)E(×), E(×)	E(√)E(√), E(√)	E(×)E(×), E(×)	O(×)O(×), O(×)	O(√)O(√), O(√)
			0.4	0	0.4	0	0.4	0	0	0.4
Predicted detection efficiency				**Incident plane//[1-10] P:S=1 : 0.44**				**Incident plane//[001] P:S=1.03 : 0.28**		

Table S5. The predicted detection efficiency of π orbitals. E, O and N correspond to even parity, odd parity, and no parity respectively.

π			TiO_6-[110]				TiO_6-[1-10]			
	Orbitals		Incident plane//[1-10]		Incident plane//[001]		Incident plane//[1-10]		Incident plane//[001]	
$1T_{2g}$	Ti	O	P(E)	S(O)	P(E)	S(O)	P(E)	S(O)	P(E)	S(O)
π1	$3d_{xy}$	$O_{1,4}$, 2px, $O_{2,3}$,2py	E(√)E(√), E(√)	E(×)E(×), E(×)	E(√)E(√), E(√)	E(×)E(×), E(×)	E(√)E(√), E(√)	E(×)E(×), E(×)	E(√)E(√), E(√)	E(×)E(×), E(×)
			0.6	0	0.6	0	0.6	0	0.6	0
π2	$3d_{yz}$	$O_{2,6}$, 2px, $O_{4,5}$,2py	N(√)N(√), N(√)	N(√)N(√), N(√)	N(√)N(√), N(√)	N(√)N(√), N(√)	N(√)N(√), N(√)	N(√)N(√), N(√)	N(√)N(√), N(√)	N(√)N(√), N(√)
			0.6	0.6	0.6	0.6	0.6	0.6	0.6	0.6
π3	$3d_{xz}$	$O_{3,5}$, 2px, $O_{1,6}$,2py	N(√)N(√), N(√)	N(√)N(√), N(√)	N(√)N(√), N(√)	N(√)N(√), N(√)	N(√)N(√), N(√)	N(√)N(√), N(√)	N(√)N(√), N(√)	N(√)N(√), N(√)
$3T_{1u}$			0.6	0.6	0.6	0.6	0.6	0.6	0.6	0.6
π4	4px	$O_{2,6}$, 2py, $O_{4,5}$, 2px	N(√)N(√), N(√)	N(√)N(√), N(√)	N(√)N(√), N(√)	N(√)N(√), N(√)	N(√)N(√), N(√)	N(√)N(√), N(√)	E(√)E(√), E(√)	E(×)E(×), E(×)
			0.4	0.4	0.4	0.4	0.4	0.4	0.4	0
π5	4py	$O_{1,6}$, 2px, $O_{3,5}$, 2py	N(√)N(√), N(√)	N(√)N(√), N(√)	N(√)N(√), N(√)	N(√)N(√), N(√)	N(√)N(√), N(√)	N(√)N(√), N(√)	E(√)E(√), E(√)	E(×)E(×), E(×)
			0.4	0.4	0.4	0.4	0.4	0.4	0.4	0
π6	4pz	$O_{1,4}$, 2py, $O_{2,3}$, 2px	E(√)E(√), E(√)	E(×)E(×), E(×)	E(√)E(√), E(√)	E(×)E(×), E(×)	E(√)E(√), E(√)	E(×)E(×), E(×)	O(×)O(×), O(×)	O(√)O(√), O(√)
			0.4	0	0.4	0	0.4	0	0	0.4
Predicted detection efficiency			**Incident plane//[1-10] P:S=0.94 : 0.63**				**Incident plane//[001] P:S=0.88 : 0.56**			

Table S6. The predicted detection efficiency of P_π orbitals. E, O and N correspond to even parity, odd parity, and no parity respectively.

P_π	**T_{2u}/T_{1g}**		TiO_6-[110]				TiO_6-[1-10]			
	Orbitals		Incident plane//[1-10]		Incident plane//[001]		Incident plane//[1-10]		Incident plane//[001]	
	Ti	O	P(E)	S(O)	P(E)	S(O)	P(E)	S(O)	P(E)	S(O)
$P_\pi 1$		$O_{1,4}$, 2py, $O_{2,3}$, 2px	E(√) E(√)	E(×) E(×)	O(×) O(×)	O(√) O(√)	E(√) E(√)	E(×) E(×)	E(√) E(√)	E(×) E(×)
			0.414	0	0	0.414	0.414	0	0.414	0
$P_\pi 2$		$O_{1,6}$, 2px, $O_{3,5}$, 2py	N(√) N(√)	N(√) N(√)	N(√) N(√)	N(√) N(√)	N(√) N(√)	N(√) N(√)	N(√) N(√)	N(√) N(√)
			0.414	0.414	0.414	0.414	0.414	0.414	0.414	0.414
$P_\pi 3$		$O_{2,6}$, 2py, $O_{4,5}$, 2px	N(√) N(√)	N(√) N(√)	N(√) N(√)	N(√) N(√)	N(√) N(√)	N(√) N(√)	N(√) N(√)	N(√) N(√)
			0.414	0.414	0.414	0.414	0.414	0.414	0.414	0.414
Predicted detection efficiency			**Incident plane//[1-10] P:S=0.39 : 0.26**				**Incident plane//[001] P:S=0.32 : 0.32**			

Table S7. The predicted detection efficiency of band gap state. E, O and N correspond to even parity, odd parity, and no parity respectively.

Band Gap States		TiO_6-[110]				TiO_6-[1-10]			
Orbitals		Incident plane//[1-10]		Incident plane//[001]		Incident plane//[1-10]		Incident plane//[001]	
Ti	O	P(E)	S(O)	P(E)	S(O)	P(E)	S(O)	P(E)	S(O)
$3d_{xy}$		E(√) E(√)	E(×) E(×)	E(√) E(√)	E(×) E(×)	E(√) E(√)	E(×) E(×)	E(√) E(√)	E(×) E(×)
		0.09	0	0.09	0	0.09	0	0.09	0
Predicted detection efficiency		**Incident plane//[1-10] P:S=0.03 : 0**				**Incident plane//[001] P:S=0.03 : 0**			

References:

(1) Cotton, F. A. *Chemical Applications of Group Theory*; John Wiley & Sons, New York City, **1991**.

(2) Liu, Y. P.; Qiu, Z. Z.; Carvalho, A.; Bao, Y.; Xu, H.; Tan, S. J. R.; Liu, W.; Neto, A. H. C.; Loh, K. P.; Lu, J. Gate-Tunable Giant Stark Effect in Few-Layer Black Phosphorus. *Nano. Lett.* **2017**, *17*, 1970-1977.

(3) Zhang, Z., et al. Direct Observation of Band Gap Renormalization in Layered Indium Selenide. *ACS. Nano.* **2019**, *13*, 13486-13491.

(4) Fischer, S.; Martín-Gago, J. A.; Román, E.; Schierbaum, K. D.; de Segovia, J. L. The valence-band electronic structure of clean and Pt-covered TiO_2(110) surfaces studied with photoemission spectroscopy. *J. Electron. Spectros. Relat. Phenomena.* **1997**, *83*, 217-225.

(5) Hardman, P. J.; Raikar, G. N.; Muryn, C. A.; van der Laan, G.; Wincott, P. L.; Thornton, G.; Bullett, D. W.; Dale, P. A. Valence-band structure of TiO_2 along the Γ-Δ-X and Γ-Σ-M directions. *Phys. Rev. B* **1994**, *49*, 7170-7177.

(6) Wang, Z., et al. Localized Excitation of Ti^{3+} Ions in the Photoabsorption and Photocatalytic Activity of Reduced Rutile TiO_2. *J. Am. Chem. Soc.* **2015**, *137*, 9146-9152.

(7) Tisdale, W. A.; Williams, K. J.; Timp, B. A.; Norris, D. J.; Aydil, E. S.; Zhu, X. Y. Hot-Electron Transfer from Semiconductor Nanocrystals. *Science.* **2010**, *328*, 1543-1547.

(8) Raikar, G. N.; Hardman, P. J.; Muryn, C. A.; van der Laan, G.; Wincott, P. L.; Thornton, G.; Bullett, D. W. VALANCE-BAND STRUCTURE OF TiO_2 ALONG THE Γ-∑-M Line. *Solid State Commun.* **1991**, *80*, 423-426.